In-Situ Synchrotron Radiation Study of Formation and Growth of Crystalline Ce$_x$Zr$_{1−x}$O$_2$ Nanoparticles Synthesized in Supercritical Water

Christoffer Tyrsted,[†] Jacob Becker,[†] Peter Hald,[†] Martin Bremholm,[†] Jan Skov Pedersen,[†] Jacques Chevallier,[‡] Yngve Cerenius,[§] Steen B. Iversen,[⊥] and Bo B. Iversen*,[†]

[†]*Center for Materials Crystallography, Department of Chemistry and iNANO, Aarhus University, DK-8000, Denmark,* [‡]*Department of Physics, Aarhus University, DK-8000, Denmark,* [§]*MAX-lab synchrotron, Beamline ID711, S-22100 Lund, Sweden, and* [⊥]*SCF Technologies a/s, Smedeholm 13B, DK-2730 Herlev, Denmark*

In situ synchrotron powder X-ray diffraction (PXRD) measurements have been conducted to follow the nucleation and growth of crystalline Ce$_x$Zr$_{1−x}$O$_2$ nanoparticles synthesized in supercritical water with a full substitution variation (x = 0, 0.2, 0.5, 0.8, and 1.0). Direction-dependent growth curves are determined and described using reaction kinetic models. A distinct change in growth kinetics is observed with increasing cerium content. For x = 0.8 and 1.0 (high cerium content), the growth is initially limited by the surface reaction kinetics; however, at a size of ∼6 nm, the growth changes and becomes limited by the diffusion of monomers toward the surface. For x = 0 and 0.2, the opposite behavior is observed with the growth initially being limited by diffusion (up to ∼3.5 nm) and later by the surface reaction kinetics. Thus, although a continuous solid solution can be obtained for the ceria−zirconia system, the growth of ceria and zirconia nanoparticles is fundamentally different under supercritical water conditions. For comparison, ex situ synthesis has also been performed using an in-house supercritical flow reactor. The resulting samples were analyzed using PXRD, small-angle X-ray scattering (SAXS), and transmission electron microscopy (TEM). The nanoparticles with x = 0, 0.2, and 0.5 have very low polydispersities. The sizes range from 4 nm to 7 nm, and the particles exhibit a reversibly pH-dependent agglomeration.

Introduction

The complex crystallographic behavior observed when mixing ceria and zirconia is well-known, and the mixed solid-state materials exhibit massive potential in a wide range of technologies such as ceramics,[1] catalysis,[2,3] solid-state fuel cell technology,[4,5] and gas sensor applications.[6,7] Conventional synthesis of Ce$_x$Zr$_{1−x}$O$_2$ usually involves methods such as high-temperature solid-state synthesis,[8] high-energy vibratory ball milling,[9] and co-precipitation with aging of solutions.[10] However, for fast synthesis and product control, these methods are not the most favorable.[11] On the other hand, hydrothermal techniques have experienced rapid growth, including solvothermal batch synthesis of Ce$_x$Zr$_{1−x}$O$_2$.[12] Large-scale production of nanoparticles in high-volume batch reactors without the use of organic stabilizers has a tendency to produce particles that are rather polydisperse.[13] On the other hand, continuous flow synthesis has the capability to produce large quantities of nanoparticles with low polydispersity and excellent control over the particle size.[13] Indeed, flow synthesis of the entire nanoceramic phase diagram of ceria, yttria, and zirconia was recently reported.[14] In the case of yttria, continuous flow synthesis in supercritical water has also been reported.[15] Poliakoff and co-workers have studied the flow synthesis of Ce$_x$Zr$_{1−x}$O$_2$ in water under subcritical conditions,[11,16]

*Author to whom correspondence should be addressed. E-mail: bo@chem.au.dk.

(1) Bocanegra-Bernal, M. H.; Torre, S. D. *J. Mater. Sci.* **2002,** *37,* 4947–4971.
(2) Kaspar, J.; Fornasiero, P.; Graziani, M. *Catal. Today* **1999,** *50,* 285–298.
(3) Kaspar, J.; Fornasiero, P. *J. Solid State Chem.* **2003,** *171,* 19–29.
(4) Mizutani, Y.; Hisada, K.; Ukai, K.; Sumi, H.; Yokoyama, M.; Nakamura, Y.; Yamamoto, O. *J. Alloys Cmpd.* **2006,** *408−412,* 518–524.
(5) Ralph, J. M.; Schoeler, A. C.; Krumpelt, M. *J. Mater. Sci.* **2001,** *36,* 1161–1172.
(6) Maskell, W. C. *Solid State Ionics* **2000,** *134,* 43–50.
(7) Lee, J.-H. *J. Mater. Sci.* **2003,** *38,* 4247–4257.
(8) Yashima, M.; Morimoto, K.; Yoshimura, M. *J. Am. Ceram. Soc.* **1993,** *76,* 1745–1750.
(9) de Leitenburg, C.; Trovarelli, A.; Zamar, F.; Maschio, G.; Dolcetti, G.; Llorca, J. *J. Chem. Soc. Chem. Commun.* **1995,** *21,* 2181.
(10) Djurcic, D.; Mcgarry, D.; Pickering, S. *J. Mater. Sci. Lett.* **1993,** *16,* 1320.

(11) Cabañas, A.; Darr, J. A.; Lester, E; Poliakoff, M. *J. Mater. Chem.* **2001,** *11,* 561–568.
(12) Devaraju, M. K.; Liu, X.; Yusuke, K.; Yin, S.; Sato, T. *Nanotechnology* **2009,** *20,* 405606.
(13) Hald, P.; Becker, J.; Bremholm, M.; Pedersen, J. S.; Chevallier, J.; Iversen, S. B.; Iversen, B. B. *J. Solid State Chem.* **2006,** *179,* 2674–2680.
(14) Weng, X.; Cockcroft, J. K.; Hyett, G.; Vickers, M.; Boldrin, P.; Tang, C. C.; Thompson, S. P.; Parker, J. E.; Knowles, J. C.; Rehman, I.; Parkin, I.; Evans, J. R. G.; Darr, J. A. *J. Combin. Chem.* **2009,** *5,* 829–834.
(15) Hayashi, H.; Ueda, A.; Suino, A.; Hiro, K.; Hakuta, Y. *J. Solid State Chem.* **2009,** DOI:10.1016/j.jssc.2009.08.013.
(16) Cabañas, A; Darr, J. A.; Lester, E.; Poliakoff, M. *Chem. Commun.* **2000,** *11,* 901–902.

and, for a thorough discussion of the $Ce_xZr_{1-x}O_2$ system, we also refer to the work of Di Monte and Kašpar.[17]

Until recently, the understanding of supercritical flow reactions has been obtained from ex situ studies, where the details of the chemical process leading to nanoparticle formation and growth were inferred from the properties of the acquired product. Using high-intensity synchrotron radiation as a probe, we have developed in situ reactors capable of opening the "black box" and studying the reactions as they happen.[18] The main challenge has been to develop reactors that can sustain the high pressures and temperatures involved for supercritical water, while allowing sufficient penetration of the X-rays to provide adequate signal-to-noise ratios on dilute suspensions of nanoparticles. The in situ information gained by combined synchrotron SAXS/WAXS studies of supercritical fluid reactions, for example, has led to the development of a procedure for large-scale synthesis of superparamagnetic magnetite nanoparticles.[19] Here, we report on synchrotron in situ studies of the synthesis of nanocrystalline $Ce_xZr_{1-x}O_2$ solid-state solutions in supercritical water. The experimental setup was constructed to simulate the conditions of the in-house continuous flow reactor. The data provide fundamental and direct information on the nucleation and growth of the primary particles. To complement the in situ study, we have conducted ex situ synthesis of $Ce_xZr_{1-x}O_2$ solid-state solutions, where the samples were comprehensively characterized by powder X-ray diffraction (PXRD), transmission electron microscopy (TEM), and small-angle X-ray scattering (SAXS).

Experimental Section

Synthesis. Synthesis in supercritical media requires a specialized synthesis apparatus, which is capable of handling high temperatures and high pressures, and, furthermore, possesses high resistance to corrosion. The continuous flow synthesis apparatus used in the present study has been described by Hald et al.[13] In the continuous flow synthesis mixtures of zirconium acetate ($Zr(ac)_4$, from Sigma−Aldrich) and ammonium cerium nitrate ($[NH_4]_2Ce[NO_3]_6$, from Lancaster Synthesis) were used as received. Five synthesis runs were conducted with [Zr:Ce] ratios of [0:1], [0.2:0.8], [0.5:0.5], [0.8:0.2], and [0:1] and a total (Zr+Ce) concentration of 0.11 M. The synthesis conditions were held at 375 °C and 230 bar, which is slightly above the critical point of water (T_C = 374 °C and P_C = 221 bar).

The in situ syntheses were performed using sapphire capillaries (1.6 mm in diameter), which were pressurized to 230 bar and heated to 375 °C using a HPLC pump and a heated air flow, respectively.[18] The conditions for synthesis in the in situ study are similar to the flow synthesis apart from a slightly different heating rate and an increase in the total (Zr+Ce) concentration to 0.20 M to get a stronger signal of the WAXS data.

Characterization. For the nanoparticles synthesized ex situ using continuous flow, PXRD data were recorded on a STOE StadiP powder diffractometer. A Ge(111) single-crystal monochromator was used to produce Cu $K\alpha_1$ radiation, which was detected with a 40° position-sensitive detector. The PXRD data were used to qualitatively monitor the degree of crystallinity in the samples, identify crystalline phases, and estimate the volume-averaged particle sizes using the Scherrer method.[20] The diffraction peaks were fitted using a pseudo-Voigt profile function. The average particle size determined by PXRD is traditionally termed a volume-averaged size. One can define a number size distribution $n(D)$ that describes the number of particles with a diameter between D and $D + \mathrm{d}D$. The volume-averaged particle size is given by

$$\langle D \rangle_{\mathrm{vol}}^2 = \frac{\langle D^8 \rangle}{\langle D^6 \rangle}$$

where $\langle D^m \rangle$ is the mth moment of the number size distribution and is given as[21]

$$\langle D \rangle^m = \int D^m n(d)\, \mathrm{d}D$$

Representative samples from the synthesis runs were investigated by TEM analysis, using a Phillips Model CM20 TEM microscope working at 200 kV.

All ex situ synthesis products were investigated by SAXS using a Bruker nanoSTAR instrument.[22] A fractal model,[23] assuming polydisperse spherical particles, was used to fit the data and a Schulz−Zimm function was employed to model the number size distribution $n(D)$. A fractal dimension and a parameter describing the size of the fractals were included to take agglomeration phenomena into account. Volume-weighted size estimates were derived from the SAXS distributions using the expression previously given. In the numerical integration over the number size distribution, 100 points were used and the distribution was truncated at the average size plus 4 times the standard deviation of the distribution.

The in situ synchrotron data were measured at beamline I711,[24] at MAX-lab, Sweden, using a home-built sample stage and a Mar165 CCD detector. The single-crystal monochromator was adjusted to produce a wavelength of 0.9496 Å and the detector had a time resolution of 11.35 s per frame. All the synchrotron diffraction data were corrected for instrumental broadening using a LaB_6 standard. The anisotropic size broadening of the diffraction peaks was described using a linear combination of spherical harmonics.[25]

$$\beta_h = \frac{\lambda}{D_h \cos\theta} = \frac{\lambda}{\cos\theta} \sum_{\mathrm{lmp}} a_{\mathrm{lmp}} Y_{\mathrm{lmp}}(\Theta_h, \Phi_h)$$

For the $x = 0.0$ and 0.2 diffractograms, the sizes were described using the real spherical harmonic function $Y_{00}(\theta,\varphi)$, whereas, for the $x = 0.5$ and 0.8, the function $Y_{20}(\theta,\varphi)$ was also included. The $x = 1$ diffractograms were described using the cubic harmonics $K_{00}(\theta,\varphi)$ and $K_{41}(\theta,\varphi)$.

(17) Monte, R. d.; Kašpar, J. *J. Mater. Chem.* **2005**, *15*, 633–648.
(18) (a) Jensen, H.; Bremholm, M.; Nielsen, R. P.; Joensen, K. D; Pedersen, J. S.; Birkedal, H.; Chen, Y.-S.; Almer, J.; Søgaard, E. G.; Iversen, S. B.; Iversen, B. B. *Angew. Chem., Intl. Ed.* **2007**, *46*, 1113–1116. (b) Bremholm, M.; Jensen, H.; Iversen, S. B.; Iversen, B. B. *J. Supercrit. Fluids* **2008**, *44*, 385–390. (c) Bremholm, M.; Becker-Christensen, J.; Iversen, B. B. *Adv. Mater.* **2009**, *21*, 3572–3575.
(19) Bremholm, M.; Felicissimo, M.; Iversen, B. B. *Ang. Chem. Int. Ed.* **2009**, *26*, 4788–4791.

(20) Langford, J. I.; Louer, D. *Rep. Prog. Phys.* **1996**, *59*, 131–234.
(21) Becker, J.; Hald, P.; Bremholm, M.; Pedersen, J. S.; Chevallier, J.; Iversen, S. B.; Iversen, B. B. *ACS Nano* **2008**, *2*, 1058–1068.
(22) Pedersen, J. S. *J. Appl. Crystallogr.* **2004**, *37*, 369–380.
(23) Teixeira, J. *J. Appl. Crystallogr.* **1988**, *21*, 781–785.
(24) Cerenius, Y.; Ståhl, K.; Svensson, L. A.; Ursby, T.; Oskarsson, Å.; Albertsson, J.; Liljas, A. *J. Sync. Rad.* **2000**, *7*, 203–208.
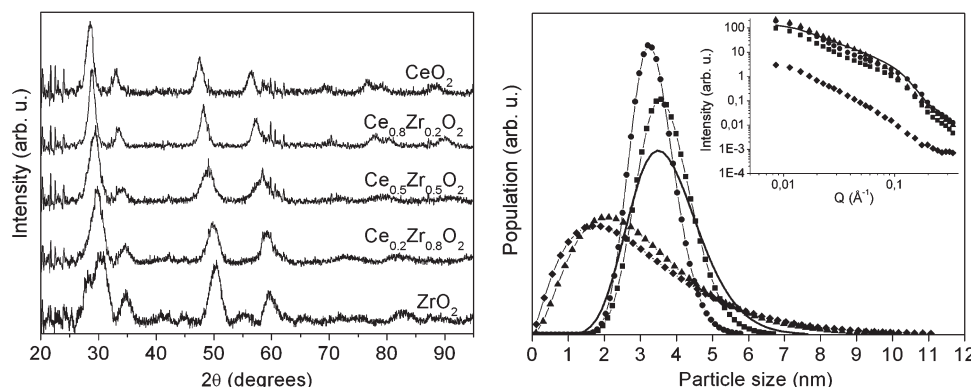(25) Jarvinen, M. *J. Appl. Crystallogr.* **1993**, *26*, 527.

Figure 1. (a) PXRD data of the $Ce_xZr_{1-x}O_2$ samples synthesized in water at 375 °C and 230 bar from mixtures of $Zr(ac)_4$ and $[NH_4]_2Ce(NO_3)_6$ precursors. (b) Size distributions and corresponding SAXS data (inset) of the as-synthesized $Ce_xZr_{1-x}O_2$ powders ((—) $x = 0.0$, (■) $x = 0.2$, (●) $x = 0.5$, (▲) $x = 0.8$, and (◆) $x = 1.0$).

Table 1. Sizes and Size Distribution Parameters of $Ce_xZr_{1-x}O_2$ Nanoparticles Obtained from PXRD and SAXS Data

	Diffraction Data				
x	angle $2\theta_B$ (deg)[a]	(hkl)[b]	PXRD $\langle D \rangle_{vol}$[c]	SAXS $\langle D \rangle_{vol}$[d]	SAXS polydispersity, z[e]
1.0	28.512	(111)	6.3	8.5	0.66
0.8	28.882	(101)	6.5	7.8	0.58
0.5	29.296	(101)	4.0	4.0	0.18
0.2	29.742	(101)	3.8	4.7	0.21
0.0	30.134	(101)	4.0	5.3	0.26

[a] $2\theta_B$ is the Bragg diffraction angle of the peak. [b] The (hkl) indices correspond to the cubic phase for $x = 1.0$ and the tetragonal phase for the remainder of the samples. [c] The parameter PXRD $\langle D \rangle_{vol}$ is the volume-averaged PXRD size estimate, which includes correction for instrumental broadening with a Gaussian model for the peak widths W (where $W_{total}^2 = W_{particle}^2 + W_{inst}^2$). [d] The parameter SAXS $\langle D \rangle_{vol}$ is the volume-averaged particle diameter, derived from the number-size distributions displayed in Figure 1b. [e] The SAXS polydispersity z is given by $z = \sigma/d_{mean}$, where d_{mean} is the number-average size and σ is the width (square root of variance) of the number size distribution displayed in Figure 1b.

Results and Discussion

Ex Situ Data. The $Ce_xZr_{1-x}O_2$ phase diagram is highly complex; it contains a monoclinic phase ($x < 0.1$), several tetragonal phases, and a cubic fluorite-type phase ($x > 0.8$), as well as several other phases at specific compositions.[26] Based on this, the $Ce_xZr_{1-x}O_2$ samples discussed here should consist of various tetragonal phases ($x = 0.2$ and 0.5), the cubic phase ($x = 1.0$), and supposedly a mixture of the two at $x = 0.8$. PXRD patterns of the $Ce_xZr_{1-x}O_2$ powders prepared in the continuous-flow reactor are shown in Figure 1a. All samples were synthesized in water at 375 °C and 230 bar from mixtures of $Zr(ac)_4$ and $[NH_4]_2Ce(NO_3)_6$ precursors. The steady progression of the peaks toward smaller angles (expanding unit cell) is evidence of cerium entering the ZrO_2 structure. The sizes of the $Ce_xZr_{1-x}O_2$ particles were obtained from the diffraction peak widths using the Scherrer formula (see Table 1).[20] The diffraction peaks of the $x = 0.2$ and $x = 0.5$ samples were difficult to fit, because of peak overlap, and the sizes may be underestimated. The size estimates obtained from the PXRD data are in good agreement with the SAXS-estimated particle sizes The SAXS values are generally larger than the Scherrer results, which may be ascribed to an amorphous outer layer on the particles.

The $Ce_xZr_{1-x}O_2$ powders for $x = 0$, 0.2, and 0.5 are very homogeneous, as can be seen from the SAXS-determined size distributions (see Figure 1). This is supported by the TEM image shown in Figure 2a for the $x = 0.5$ sample, and it has previously been observed that particles with this composition are highly resistant towards sintering.[11] This can be explained by the fact that particles of almost-identical sizes are resistant to Ostwald ripening, because it is not energetically favorable for any particle to grow at the expense of the others.

The TEM image in Figure 2b reveals that the pure CeO_2 sample contains particles of two different size regimes. The majority of these particles are in excellent agreement with the PXRD estimate, but a small fraction of the particles are in the range of 16−20 nm. This situation explains the wider size distributions of the $x = 0.8$ and $x = 1$ powders. The occurrence of the observed two particle size regimes seems to be caused by particle agglomeration during the synthesis (see below). The TEM image in Figure 2c reveal that the as-synthesized CeO_2 powder consists of large agglomerates. The particles seen in Figure 2b were not observable until these agglomerates were dispersed. The agglomeration seems to grow stronger as the value of x increases (compare Figures 2a and 2c). This suggests that the agglomeration phenomenon is linked to the pH value of the synthesis medium, because the decomposition of the nitrate cerium precursor yields nitric acid in solution, which reduces the pH value of the synthesis medium as the value of x increases.

To test the pH-dependence hypothesis, the $x = 1$ sample was washed thoroughly with water until neutral pH was

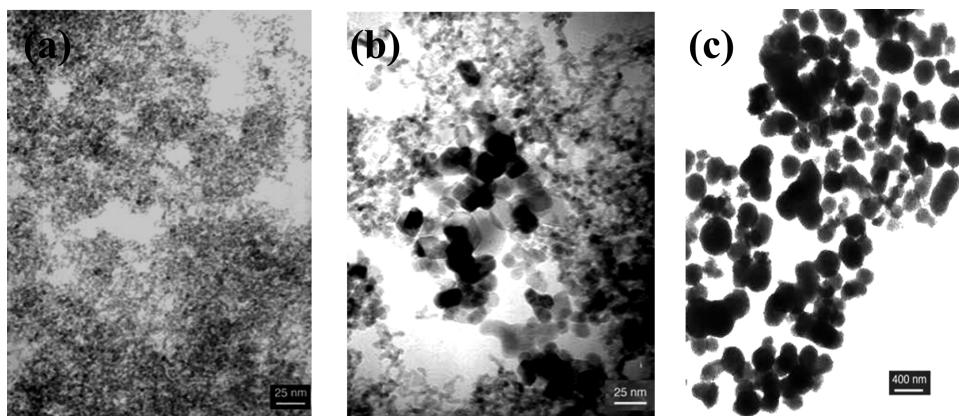(26) Adschiri, T; Yukiya, H.; Arai, K. *Ind. Eng. Chem. Res.* **2000**, *39*, 4901–4907.

Figure 2. (a) TEM micrograph of as-synthesized $Ce_{0.5}Zr_{0.5}O_2$ particles. (b) TEM micrograph of washed CeO_2 (pH 7) particles. (c) TEM micrograph of as-synthesized CeO_2 (pH 1) particles.

achieved. The impact on the degree of agglomeration is remarkable, as displayed by the difference between Figures 2b and 2c. The two size regimes of the CeO_2 particles observed in Figure 2b suggest that the agglomeration occurs on the walls on the inside of the hot flow reactor. The thermal environment causes the agglomerated particles to fuse and form the observed larger crystallites.

When cerium is introduced in the ZrO_2 matrix, the polydispersity increases (see Table 1). The increasing polydispersity toward higher values of x is an effect of the increasing degree of particle agglomeration and the corresponding greater tendency toward separate particle size regimes. Therefore, the high polydispersity value of 0.66 for $x = 1$ is caused by the 16−20 nm crystallites. The impact of this on the size distributions determined from SAXS data is seen in Figure 1. The size distributions for $x = 0.8$ and 1 are much broader and more skewed, compared to those of the other samples. This is due to the monomodal Schultz−Zimm function trying to mimic the gap between the two size regimes of the particles (6−7 nm and 16−20 nm, respectively). Despite this, the fit to the SAXS data is good and we can conclude that we do not have resolution to separate the two components of the size distribution. Since there is a connection between the pH value and the degree of agglomeration, it is expected that if the syntheses are conducted under mild alkaline conditions, the homogeneity of the resulting particles can be much improved, and the polydispersities, correspondingly, can be greatly reduced.

In Situ Data. The in situ WAXS studies were performed under conditions similar to the supercritical flow synthesis, i.e., at 375 °C and 230 bar. To obtain a good diffraction signal from the synthesis, the precursor concentration (Ce + Zr) was increased to 0.20 M. An overview of the different synthesis series is shown in Figure 3, which contains diffractograms measured after 15 min of reaction time.

Similar to that observed for the continuous-flow synthesis samples, there is a steady progression of the peaks toward smaller angles as the Ce/Zr ratio increases. The diffraction pattern for ZrO_2 corresponds to a pure monoclinic phase. A tetragonal phase is present very early in the
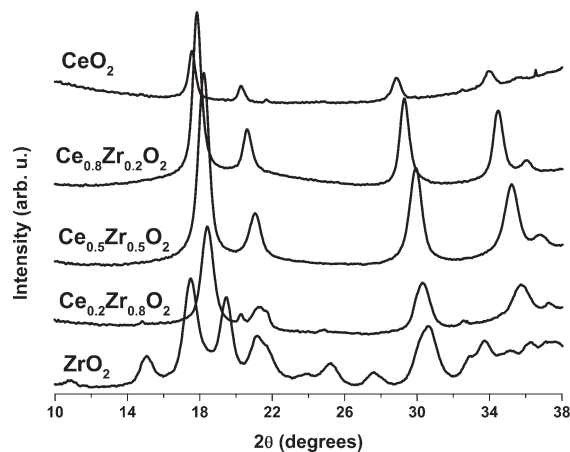

Figure 3. In situ PXRD data of the $Ce_xZr_{1−x}O_2$ samples synthesized in water at 375 °C and 230 bar. All the data were taken 15 min after initiation of the experiments.

synthesis, but it transforms to the monoclinic phase 30 s after initiation of the reaction. The diffractograms for the $x = 0.2, 0.5,$ and 0.8 samples all exhibit the tetragonal phase whereas the ceria particles are most likely to be phase-pure cubic. Because of the size broadening of the diffraction peaks, it is difficult to distinguish between the very similar tetragonal and cubic polymorphs.[17]

The time-resolved PXRD data have been analyzed using sequential Rietveld refinement. To extract the growth of the primary particles, the broadening of the diffraction peaks is modeled using spherical harmonic functions to account for the anisotropy of the Bragg peaks at different diffraction angles, which originates from nonspherical particle shape. Because the majority of the samples have ellipsoidal particle morphology, the growth is divided into two graphs. Figure 4 shows the growth along the a/b unit-cell axes, which are equivalent for all particle shapes (sphere, ellipsoid, cubic), while Figure 5 shows the growth along the c unit-cell axis. In the case of the monoclinic ZrO_2, the c-direction denotes the direction orthogonal to the (a,b)-plane. The gray lines plotted on top of the measured data points for each series is the modeled growth curves described below.

The results shown in Figures 4 and 5 reproduce the general trend in particle size found from PXRD of the
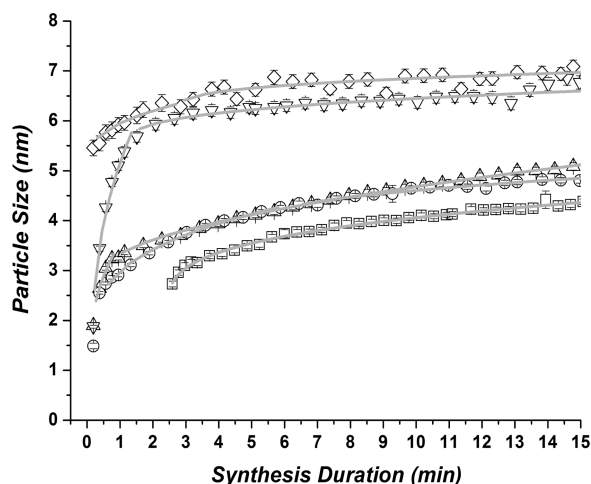
Figure 4. Time-dependent growth in the *a,b* unit-cell-axis direction of $Ce_xZr_{1-x}O_2$ powders: ($\square$) $x = 0.0$, ($\bigcirc$) $x = 0.2$, ($\triangle$) $x = 0.5$, ($\bigtriangledown$) $x = 0.8$, and ($\diamond$) $x = 1.0$. The solid gray lines correspond to the fitted *N*-exponent model. For the sake of clarity, every other data point in each series has been removed from the plot.

Figure 5. Time-dependent growth in the *c* unit-cell-axis direction of $Ce_xZr_{1-x}O_2$ powders: ($\square$) $x = 0.0$, ($\bigcirc$) $x = 0.2$, ($\triangle$) $x = 0.5$, ($\bigtriangledown$) $x = 0.8$, and ($\diamond$) $x = 1.0$. The solid gray lines correspond to the fitted *N*-exponent model. For the sake of clarity, every other data point in each series has been removed from the plot.
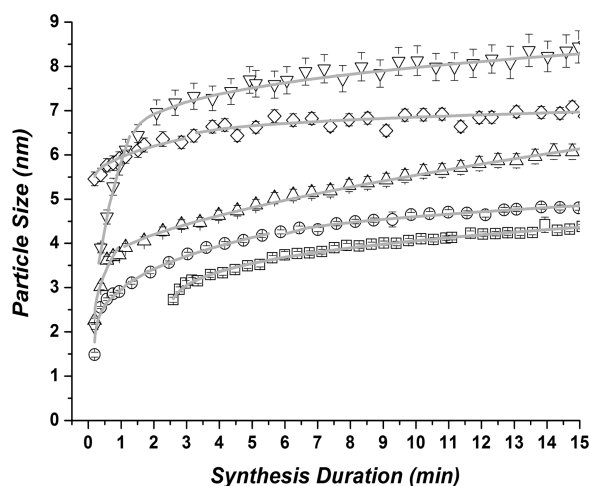
Table 2. Parameter Values for the *N*-Exponential Model for Particle Growth in the *a*- and *b*-Directions

	$D(t) = D_0 + k(t - t_0)^N$			
	First Period		Second Period	
x	t_0	N	t_0	N
1.0	0.189	0.504	2.841	0.354
0.8	0.189	0.477	1.323	0.345
0.5	0.189	0.523	0.568	0.559
0.2	0.189	0.320	6.061	0.611
0.0	2.476	0.302		

that it initially forms a hydrogel, which then transforms to individual ZrO_2 nanoparticles.

The growth of the nanoparticles often proceeds via several mechanisms, depending on the specific system and the local concentration of monomers in the solvent medium. Under these circumstances, an applicable way to extract semiquantitative information about the mechanisms is to fit the growth curves with a generalized *N*-exponential growth model: $D(t) = D_0 + k(t - t_0)^N$ where D is the diameter of the particle and t is the time.[27] Through the known values of D_0 and t_0, it is possible to extract useful information from the value of the parameter N, which is given by the fits to the growth curves. If the surface reaction between the monomers and the growing particles is fast, the growth is usually limited by diffusion of additional monomers from the surroundings to the particle surface. In this scenario, the Lifshitz−Slyozov−Wagner (LSW) theory[28] states that the volume of the particles should increase linearly with time, i.e., $N \approx \frac{1}{3}$ in the present nomenclature. If, on the other hand, the surface reaction kinetics represents the limiting factor, the surface of the particles should increase linearly with time, i.e., $N \approx \frac{1}{2}$.[27] Although different growth kinetics may influence the final size of the particles, it is usually quite easy to assign the dominant process in different domains of the growth curves. No emphasis is placed on the size of parameter k, which is heavily dependent on the microenvironment probed and has no direct influence on the parameter N. For each fit, the start parameters for D_0 and t_0 have been fixed by the actual points on the growth curves and k and N have had no constraint other than the necessity for the values to be greater than zero. The fits are shown on top of the growth curves in Figures 4 and 5. A closer examination reveals that all fits lie within the error bars of the measured data, except for at a few diverging points, and, therefore, the uncertainties on the N parameters are rather limited. None of the values for N are equal to $\frac{1}{2}$ or $\frac{1}{3}$, but a value within 10% of these predictions is a clear indication of how the growth mechanism is at this time period. The exact values of N for the fits in Figures 4 and 5 are shown in Tables 2 and 3, respectively. Except for the $x = 0$ series, the growth in all the other series are best modeled by splitting the growths into two separate time domains, abbreviated here as *first period* and *second period*, beginning at t_0 (also given in

continuous-flow synthesis (see Table 1). The particles are split into two size regimes, where the series with $x = 0$, 0.2, and 0.5 are equivalent in size and generally smaller than the particles from $x = 0.8$ and 1.0. The same trend was observed by Poliakoff et al., with one exception: their particle size for the pure zirconia is slightly bigger than that for lightly doped zirconia.[11] With the insight gained from the in situ study, it is possible to compare the kinetics in the cerium-doping series. The size in the *a*- and *b*-directions for the ceria-rich $x = 0.8$ and $x = 1$ phases reaches equilibrium ~2 min earlier than the less-ceria-doped phases ($x = 0$, 0.2, and 0.5). The same trend is observed for growth in the *c*-direction, where the $x = 0.5$ series requires more than 30 min before it converges to a size of 7 nm (not shown in Figure 5). Generally, a couple of minutes are required before the pure zirconia starts to nucleate, because it could be observed during the experiment

(27) Rao, C. N. R.; Muller, A.; Cheetham, A. K. *Nanomaterials Chemistry−Recent Developments and New Directions*; Wiley−VCH Verlag GmbH: Weinheim, Germany, 2007.
(28) Lifshitz, I. M.; Slyozov, V. V. *J. Phys. Chem. Solids* **1961**, *19*, 35–50.
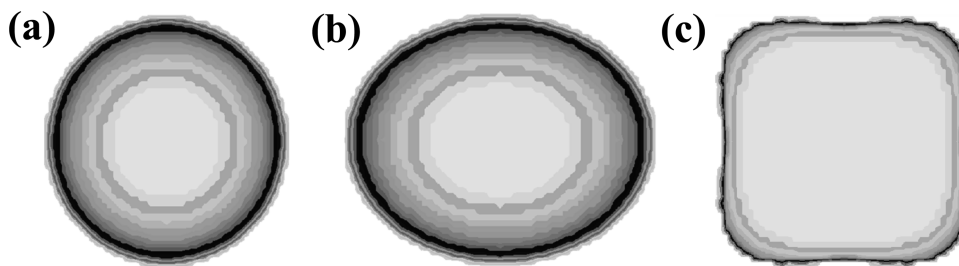
Figure 6. Cross-sectional images of (a) the (a,b)-plane for particles with $x = 0.5$, (b) the (a,c)-plane for particles with $x = 0.5$, and (c) the (a,b)-plane for particles with $x = 1.0$.

Table 3. Overview Parameter Values for the N-Exponential Model for Particle Growth in the c-Direction

	$D(t) = D_0 + k(t - t_0)^N$			
	First Period		Second Period	
x	t_0	N	t_0	N
1.0	0.189	0.504	2.841	0.354
0.8	0.189	0.512	1.326	0.352
0.5	0.189	0.515	0.568	0.635
0.2	0.189	0.320	6.061	0.611
0.0	2.476	0.302		

Tables 2 and 3). This is done because a single fit cannot be applied to the entire growth curve if large changes in the growth characteristics occur. For pure ZrO_2, the entire process can be assigned as being diffusion-limited with $N \approx 0.3$. When the doping concentration of cerium is increased to $x = 0.2$, the FIRST period of growth is limited to diffusion; however, after this time period, a new fit with $N \approx 0.6$ gives better correspondence with the data. This is a sign of the surface incorporation of monomers becoming the limiting factor, even though the value is rather far from the required $N = \frac{1}{2}$. From this point forward, when increasing the cerium content, an apparent inversion in the growth process begins to appear. The growth of the $x = 0.5$ series seems to be constituted by two similar, but not equal, surface-limited processes. The two cerium-rich series $x = 0.8$ and $x = 1.0$ both exhibit similar trends where the growth is first controlled briefly by the surface reaction, until a certain size is reached and diffusion becomes the limiting factor.

The results for the $x = 0.8$ and $x = 1.0$ series fit the general perception for particle growth very well. The growth of particles right after nucleation is usually not limited by diffusion, because the monomer concentration at the particle surface is still high. When the particles have reached a certain size, the concentration in the vicinity of the particle surface will have decreased sufficiently for the further growth to be limited by the diffusion of new monomers. Therefore, it is surprising that the $x = 0.2$ series exhibits the exact opposite behavior. This may be due to an amorphous layer that may be starting to grow on the crystalline particles, which would change the surface kinetics. However, without certain proof of this, we can only state that some sort of change in the growth mode occurs during the growth of the $x = 0.2$ particles. Aside from the natural change in crystal structure from one series to the next, the changes in growth characteristics between the series may also be explained by the increasing acidity of the solution from the cerium

precursor causing agglomeration, which affects the kinetics.

The change in cerium doping not only influences the overall particle size and growth characteristics, but also the shape of the particles. Indeed, the specific morphology of nanoparticles is often critical for their application. The spherical harmonic functions used to describe the anisotropic peak broadening can be used to visualize the particle morphologies (here, using the GFOURIER program part of the Fullprof Suite).[29] The anisotropy of the Bragg peaks for the zirconia-rich series $x = 0$ and 0.2 are negligible and the particle shapes are, consequently, best described as spherical. For the intermediate phases ($x = 0.5$ and 0.8), the anisotropy is significant and was modeled with a prolate spheroid particle morphology, where the size in the c-direction is longer than the equivalent a,b-directions. The size ratio (c/a) for these two series increases slightly from 1.21 to 1.27 when increasing the ceria content. In Figure 6, the particle shape is shown for $x = 0.5$ in the (a,b)-plane and (a,c)-plane. For pure CeO_2 the particles exhibit a cubic morphology in fine correspondence with earlier studies (see Figure 6c).[30] As such, there is a trend in the particle morphology when changing the Ce/Zr ratio, similar to that which has been shown for the general sizes in Figures 4 and 5. The pure zirconia particles exhibit no preferred direction of growth. This changes when the doping of ceria increases. As explained previously for $x = 0.5$ and 0.8, the growth is faster in the longer unit-cell-axis c-direction before the pure ceria particles distinguish themselves with a cubic morphology.

Conclusion

Continuous-flow synthesis of $Ce_xZr_{1-x}O_2$ for $x = 0$, 0.2, and 0.5, in supercritical water, produces nanocrystalline particles with a narrow size distribution of ~ 2–3 nm (full width at half maximum (fwhm), as shown by small-angle X-ray scattering (SAXS) and transmission electron microscopy (TEM)). Samples with $x = 0.8$ and 1.0 have considerably higher polydispersity, because of the occurrence of bimodal size distributions. TEM images reveal a pH-dependent agglomeration, which increases with increasing amounts of the acidic ceria precursor. The agglomeration is a reversible process, and the soft agglomerates

(29) Rodriguez-Carvajal, J. *Physica B* **1993**, *192*, 55.
(30) Ge, M. Y.; Wang, H.; Liu, E. Z.; Liu, J. F.; Jiang, J. Z.; Li, Y. K.; Xu, Z. A.; Li, H. Y. *Appl. Phys. Lett.* **2008**, *93*, 062505.

can be dispersed by increasing the pH level. At high cerium concentrations, the average particle size increases from ~4 nm to ~6 nm. In situ synchrotron WAXS measurements reveal that the particle growth is anisotropic with increasingly ellipsoidal particles (the *c*-axis is longer than the *a*- and *b*-axes) as *x* increases. At $x = 1$ (i.e., pure CeO_2), the particle shape becomes cubic. Reaction kinetics derived from fits to the experimentally determined nanoparticle growth curves reveal a fundamental change in growth mechanism when going from zirconium-rich to cerium-rich phases. In the cerium-rich part of the phase diagram, the particle growth is initially limited by surface reaction kinetics; however, at a size of ~6 nm, the growth changes and becomes limited by the diffusion of monomers to the surface. In the zirconium-rich part of the phase diagram, it is observed that the initial growth of small particles is limited by diffusion. The growth mechanism changes at a particle size

of ~3.5 nm, where the growth becomes limited by the surface reaction kinetics. The latter may be due to the formation of an amorphous surface layer, which limits the crystalline growth monitored by PXRD. The differences in initial growth kinetics of the CeO_2 and ZrO_2 phases may also be the origin of the much-faster initial growth of CeO_2 nanoparticles, compared to ZrO_2 nanoparticles in supercritical water.